



Castability of Cu-Al-Mn shape memory alloy in a rapid investment casting process: computational and experimental analysis

Carlos Eduardo da Silva Albuquerque¹ · Estephanie Nobre Dantas Grassi² · Carlos José De Araújo²

Received: 21 December 2022 / Accepted: 23 May 2023 / Published online: 5 June 2023
© The Author(s), under exclusive licence to Springer-Verlag London Ltd., part of Springer Nature 2023

Abstract

Comparisons between virtual prototyping and experimental results are notably beneficial for the development of investment casting processes. In this research, such a comparison aimed to study the castability of a Cu-Al-Mn shape memory alloy (SMA) in a modified centrifugal investment casting process that uses centrifugal force to inject the molten metal into the mold. Virtual prototyping was numerically simulated using the ProCAST software applying a rectangular mesh part design. The real and virtual parts were examined for mold filling (castability), pore formation, and solidification time. Using Whitlook's methodology, it was possible to validate the model created in the ProCAST software to simulate the modified investment casting process, detecting results regarding filling, solidification, and porosity with a high degree of accuracy and reliability. In addition to the validation of the developed model, this work also presents estimated values for interface heat transfer coefficient (IHTC) of the metal/mold of aluminum bronze (Cu-Al and Cu-Al-Mn) alloys poured by gravity and centrifugation into plaster molds. Among the obtained values, the IHTC for the 86.7Cu-7.9Al-5.4Mn SMA were estimated at 535 W/m² K when poured by centrifugal force and 75 W/m² K by gravity. Ultimately, it was possible to verify that Cu-Al-based shape memory alloy presents a high castability and a low cooling rate.

Keywords Casting · Investment casting · Shape memory alloys · Cu-Al-Mn alloy · Casting numerical simulation · ProCAST software

1 Introduction

Shape memory alloys (SMA) belong to a class of metals known as smart or intelligent materials, a state-of-the-art metallic alloy that has been developed and applied in various sectors over the last decades. The continuous study and development of manufacturing and processing routes to

obtain such advanced materials make them increasingly accessible and reliable, which widens the application range for many present and future technologies. SMA present a diffusionless reversible solid-solid thermoelastic phase transformations between a stable higher temperature austenite phase and a lower temperature martensite phase. These reversible transformations are responsible for giving rise to interesting phenomena: the shape memory effect (SME) and superelasticity (SE). The former (SME) is the ability to return to a predetermined shape upon simple heating, and the latter (SE) is the ability to recover large strains (~8% under tension) upon unloading under isothermal conditions [1]. Due to these specific phenomena, SMA have attracted much interest for a wide range of applications, such as aerospace [2, 3], medical-dental [4–6], automotive [7, 8], and civil construction [9].

In general, it is possible to state that there are two main classes of SMA: Ni-Ti-based alloys (Ni-Ti, Ni-Ti-Cu, Ni-Ti-Mo, Ni-Ti-Nb, etc.) and copper-based alloys (Cu-Zn-Al, Cu-Al-Ni, Cu-Al-Mn, Cu-Al-Be, etc.).

✉ Carlos Eduardo da Silva Albuquerque
carlos.albuquerque@univasf.edu.br

Estephanie Nobre Dantas Grassi
end.grassi@hotmail.com

Carlos José De Araújo
carlos.jose@professor.ufcg.edu.br

¹ Universidade Federal do Vale do São Francisco Rua Antônio Figueira, 134, Nossa Senhora das Graças, Salgueiro PE CEP: 56000-000, Brazil

² Universidade Federal de Campina Grande Rua Aprígio Veloso, 882, Universitário, PB CEP, Campina Grande 58429-900, Brazil

Cu-Al-based SMA feature not only the functional characteristics of SME and SE but also a lower cost and ease of manufacture when compared to Ni-Ti-based alloys [10].

Agrawal and Dube [11] have recently described some manufacturing processes used for Cu-Al-Ni SMA, emphasizing that casting methods are the most commonly used processes. Depending on the particularities of the casting process, it can be named investment casting, gravity casting, die casting, sand casting, centrifugal casting, among others. Regardless of the classification of the casting process, all are subject to design and processing errors at some stage, but the correct identification of defects in the initial phase significantly reduces the probability of product failure.

There are different ways to analyze the phenomena that occur in a casting process, among which we highlight real casting tests and numerical simulation of casting processes. Because it is much faster and cheaper than real casting tests, analyzing the casting process by means of numerical simulation has become a very viable and advantageous approach [12, 13].

Numerical simulation makes it possible, through a computational model, to represent the real physical problem and to conduct virtual experiments that enable the understanding of how the process will respond to changes in some of its variables. In addition to allowing the study of real systems without modifying them, this tool grants a better understanding of which variables are most important regarding performance, how they interact with each other and with the other elements of the system, and allows the accurate replication and analysis of extreme conditions with confidence. Specifically for the case of virtual casting analysis through numerical simulation, the filling processes, solidification, defect formation, and distribution during the casting process can be predicted, avoiding unnecessary raw material expenses, labor, energy, and other resources [13].

Recently, Kumar et al. [14] carried out a study using numerical simulation of the investment casting process to manufacture a part with a complex design and a high degree of finishing, called a rotating adapter. In their study, the Unigraphics® software was used to build the physical model of the part and the ProCAST® software was used to simulate the pouring, heat exchange, and solidification processes. Simulations were carried out to analyze and identify defects, allowing for the design and implementation of a different blocking system to eliminate these identified defects. The process was repeated in the ProCAST® software with the efficiency having been proven by obtaining a casting no defects. Dou et al. [15] developed a numerical simulation approach also based on the ProCAST® finite element casting software, having carried out a study of fluid flow, solidification and defect formation during each stage of the high-pressure casting process: casting, injection and cooling. Air trapping and porosity distribution in the casting

were foreseen. Alisson et al. [16] described in one of their works the virtual aluminum casting methodology, which was developed and implemented at Ford Motor Company, where the so-called virtual foundries are carried out. Using the ProCAST® and Abaqus® software, the only inputs to the calculation used were the complex geometry of the matrix, the alloy composition, and the required properties. Castability, phase transformations, and resulting mechanical properties (tensile strength and low cycle fatigue properties) were simulated in the same 3D virtual domain. The Ford company claimed that this new approach reduced the time for designing new engine blocks by 15–20% and therefore saved millions of dollars.

An accurate and reliable numerical simulation depends on a good discretization of the studied domain, model accuracy, evaluation methodology, technical knowledge of the involved physic phenomena, and input data of precise, self-consistent and realistic thermophysical properties. In addition to these requirements, the numerical simulation of a casting process requires the knowledge of some important parameters, especially the metal/mold interface heat transfer coefficient (IHTC). The availability of values for this specific heat transfer coefficient in the literature is relatively scarce, and the high diversity characteristics of metal/mold systems imply the need to develop methodologies for its experimental determination [17].

In this context, this work presents a computational and experimental analysis of a rapid investment casting process, which uses centrifugal force to inject the molten metal into refractory plaster molds obtained from resin models using 3D printing. The computational analysis presented in this study was carried out using the ProCAST® software, and the real parts were manufactured following the standard casting method proposed by Whitlock and Hinman [18]. With this analysis, it was possible to evaluate the influence of the alloy and the injection temperature on the casting of the manufactured parts. The concept of “castability” adopted in this work consists of filling a mold in the form of a net, as will be detailed later. In addition to this analysis, this work presents important data on the metal/mold interface heat transfer coefficient for Cu-Al-Mn SMA, a parameter that directly influences the filling capacity of the mold details.

2 Experimental methodology

This work will be based on numerical simulations and physical experiments in order to perform the analysis of an investment casting process applied to manufacturing of miniaturized parts of aluminum bronzes with functional properties (SME and/or SE) based on a Cu-Al-Mn SMA.

The following main parameters of the process will be evaluated: mold filling, porosity formation, temperature

gradients inside the part, and solidification time. The manufacturing process of miniaturized parts of aluminum bronze alloys using centrifugal force to fill the mold is the main process studied in this research. However, due to difficulties to access the interior of the equipment during the melting and injection, and due to the rotation of the casting arm, crucible, and mold, the direct determination of the heat transfer coefficient between the metal and the mold in this process becomes a challenging task. Knowing that the IHTC between the metal and the mold is an essential parameter to obtain accurate numerical results, it was necessary to design a complementary experiment. Therefore, in the experimental part of this work, besides the centrifugal injection method, a casting with gravity potential energy to fill the mold was applied solely to allow the estimation of the IHTC. The two casting experimental methodologies differ only by the pouring method.

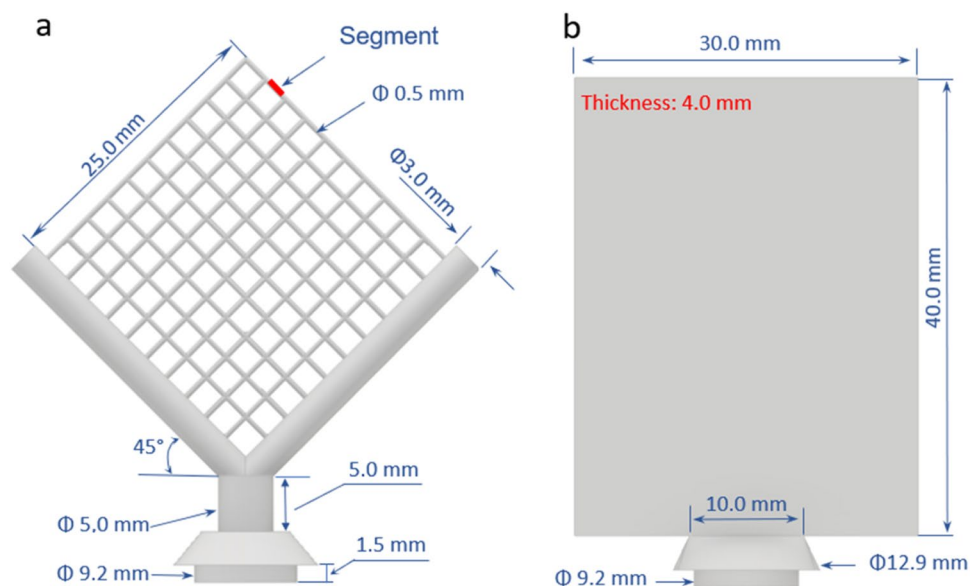
In this study, three different compositions of Cu-Al-based SMA were evaluated in order to verify the influence of each component on the ability to fill the details of the mechanical part and on the formation of defects. The alloys were fabricated using an open, unshielded, gravity-filled induction melting furnace using a steel metallic mold.

Table 1 shows the chemical compositions in weight percentage of the alloys. In this table, alloys 1 and 2 are conventional aluminum bronzes and the alloy 3 is a Cu-Al-Mn shape memory alloy. At room temperature, this SMA is in a

Table 1 Chemical composition (%wt) of the Cu-Al-based alloys

Alloy	Cu	Al	Mn
1	99.95	0.05	-
2	98.40	1.60	-
3	86.70	7.90	5.40

Fig. 1 CAD design of the studied parts. **a** Y 2D lattice based on Whitlock methodology. **b** Plate model used to estimate the metal/mold IHTC by gravity casting



mixed state of martensite and austenite, as determined by a differential scanning calorimetry (DSC) analysis. The phase transition temperatures of the alloy, which determine if the SE or SME occur at a given temperature, were $M_f = -28.33$ °C, $M_s = 6.22$ °C, $A_s = 9.81$ °C, and $A_f = 58.18$ °C.

The first step to manufacture a mechanical part through the process under study is to obtain a model of the desired part. In this work, resin models are obtained by rapid prototyping using a 3D printer (AnyCubic, Photon model). The CAD models generated for printing have the same dimensions as the models used for computational simulations. Figure 1 shows the CAD lattice geometry (Fig. 1a) used to compare the virtual prototyping cases with the real ones and the plate model used in the IHTC estimation (Fig. 1b). The Y 2D lattice design was created based on the Whitlock methodology used to study casting of dental alloys [18, 19].

After printing the resin models according to Fig. 1, the molds are manufactured using ResinCast refractory plaster with a water/powder ratio of 38 ml:100 g following the sintering curve shown in Fig. 2.

2.1 Pouring by gravity to determine IHTC

The gravity pouring process illustrated in Fig. 3 starts with melting the alloys in an open induction melting furnace (H). The melting and gravity pouring process is done individually for each composition of Table 1. After the alloy reaches the desired temperature, the molten alloy is poured from the crucible (G) to the mold prepared with the thermocouples (F). The pouring process takes approximately 2 s.

Four thermocouples were used, one positioned in the center of the part and the other 3 distributed inside the mold at approximately 4 mm, 14 mm, and 24 mm from the center of the mold (schematic shown in Fig. 4). The thermocouples

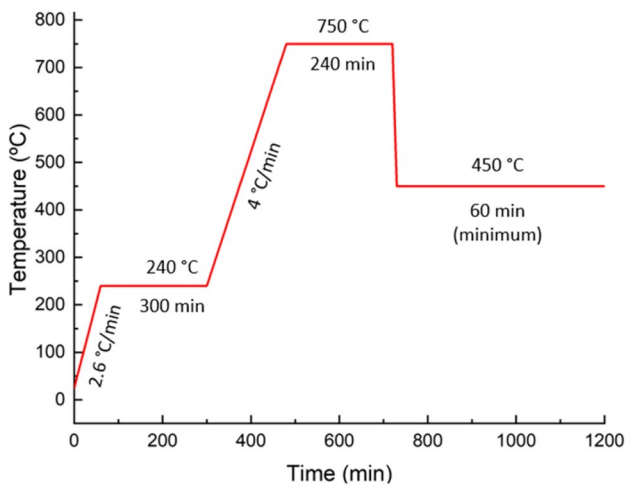


Fig. 2 Sintering profile used to prepare the Resin-cast plaster molds

were named T00, T02, T12, and T22 in reference to their distance from the metal/mold interface (excluding T00, which was named in reference to the center of the mold).

The thermocouples used are K-type (Cromel-Alumel) with a diameter of 100 μm. It allows measurements between −220 and 1260 °C with a sensitivity of approximately 41 μV/°C. To preserve the integrity and guarantee the correct acquisition of the temperature inside the part, the T00 thermocouple, which was in direct contact with the molten alloy, was encapsulated. Temperatures are read using an Agilent 34970A data logger. After acquiring the temperatures for the 3 alloys, the data were processed and it was possible to estimate the IHTC value for each alloy and mold material. These values are used as initial inputs in the simulations with ProCAST to allow the definition of the final value of the IHTC for the assembly.

Fig. 3 Experimental setup to determine the IHTC by gravity pouring

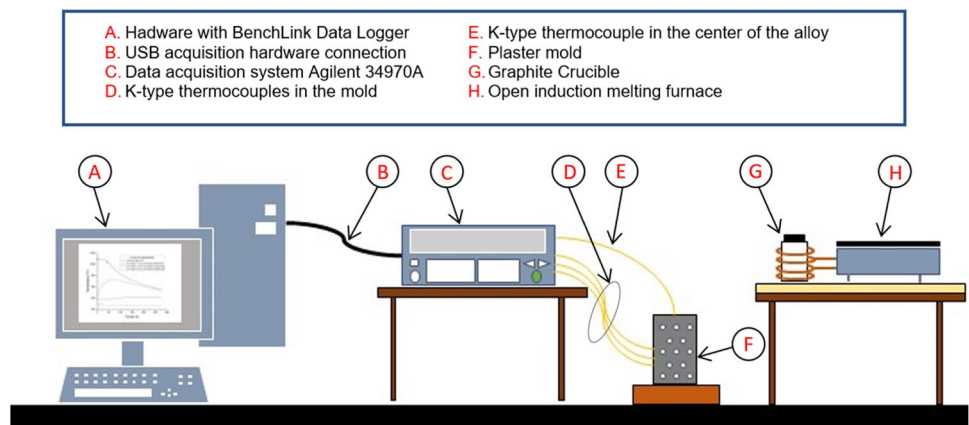
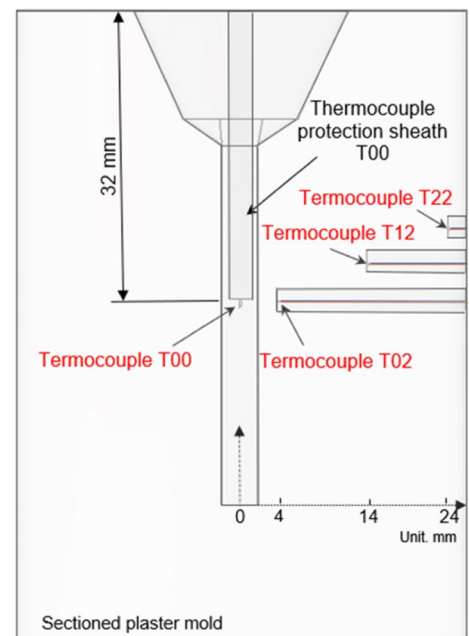


Fig. 4 Positioning of thermocouples in the alloy and mold



The calculations were based on the fact that the IHTC, h_i , depends on the heat flow from the molten to the mold across the interface, q_N , and on the temperature drop ΔT at the interface, as numerically described as follows [17]:

$$q_N = h_i(T_{is} - T_{im}) \tag{1}$$

The total heat flux, q_N , at the metal/mold interface consists of the sum of the flux that the melt loses to the mold, q_c , and the flux due to the exothermic nature of solidification, q_s [20]. The flow q_c is calculated by decreasing the temperature in the considered volume, as shown below:

$$q_c(t) = \frac{\rho_f \chi c_p [T(t) - T(t + \Delta t)]}{\Delta t} \tag{2}$$

And the flux q_s due to the exothermic nature of solidification is assumed to decrease linearly in the solidification interval and is calculated as follows [20]:

$$q_s(t) = \frac{2\{1 - [(t - t_{liquid}) / (t_{solid} - t_{liquid})]\} \rho_f \chi E_s}{\Delta t} (t_{liquid} \leq t \leq t_{solid}) \tag{3}$$

where ρ_f is the density of the melt, χ is half the thickness of the plate, c_p is the heat capacity of the melt, $T(t)$ is the temperature at time t , t is the time increment, E_s is the latent heat of the alloy, t_{liquid} is the beginning of solidification, and t_{solid} is the end of solidification.

The alloy properties required to feed Eqs. (2) and (3) were calculated by ProCAST via the right link to the CompuTherm database. The time increment used was 0.17 s. For the calculation, some simplifications were made: heat is only transported perpendicular to the mold surface; the heat transfer in the melt is infinitely high; constant mold thermal conductivity; temperature propagation is linear due to constant thermal conductivity in the mold; solidification energy decreases linearly during solidification. Taking these simplifications into account, it was considered that the heat transfer in the alloy is much faster than in the mold. Therefore, it is assumed that the temperature measured by the thermocouple T00 in the center of the mold (Fig. 4) is uniform throughout the alloy. The temperature on the mold side of the metal/mold interface was estimated by linear extrapolation of the temperatures measured by thermocouples T02, T12, and T22. The difference between these temperatures at the interface is the temperature drop ΔT . The temperature at the interface is then determined by the extrapolation procedure for each time step in the solidification interval and thus the heat transfer coefficient can also be calculated directly from Eqs. (1), (2), and (3) for each time step.

Figure 5 shows the determination of the temperature drop ΔT at the alloy/mold interface (example for time node $t = 32$ s).

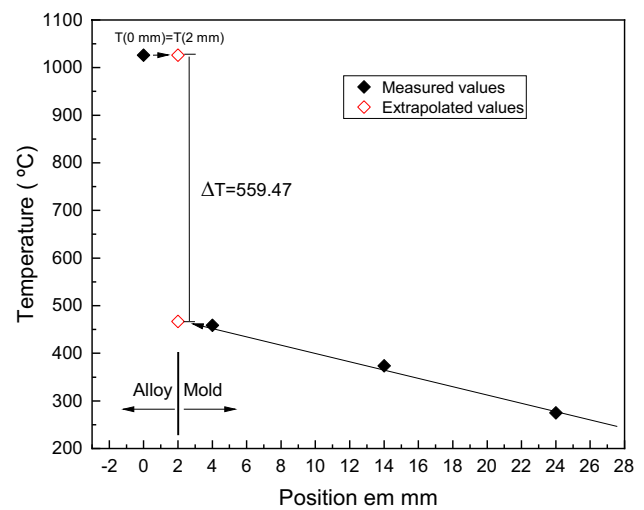


Fig. 5 Determination of the temperature drop ΔT at the alloy/mold interface at $t = 32$ s for the Cu-Al-Mn SMA

2.2 Injection by centrifugal force

The manufacturing process of the miniaturized parts of Cu-Al-Mn SMA studied in this work (Fig. 1a) uses centrifugal force to fill the molten alloy into the mold. The PowerCast 1700 machine, supplied by EDG Equipamentos e Controles (Brazil), was employed. Figure 6 shows a picture of this machine and illustrates a schematic drawing of the rotation and injection centrifugal system described by Mun et al. [21]. To carry out the centrifugal force filling, small discs of each alloy are cut from the manufactured ingots. Masses ranging from 8 to 9 g were employed, depending on the alloy. The machine has a melting capacity of up to 50 g, but the geometries studied in this research did not require loads above 9 g. These small discs are placed in a ceramic crucible installed on the crucible holder.

The plaster mold is then removed from the oven at 450 °C and inserted into the mold cradle. Once the mold is in place, the mold cradle support arm is adjusted to maintain the mold in the injection position and the casting arm is balanced by the counterweight setting. The door of the PowerCAST 1700 is manually closed, and the casting parameters such as rotation speed, acceleration, and temperature are set. When the start button is pressed, an automatic safety verification is performed and the induction coil starts heating.

After the alloy is melted, or reaches the desired heating time, the rotation lever is activated and the casting arm containing the crucible rotates at the predetermined speed, which in the case of this research was 350 rpm, for approximately 11 s, forcibly injecting the melt into the mold.

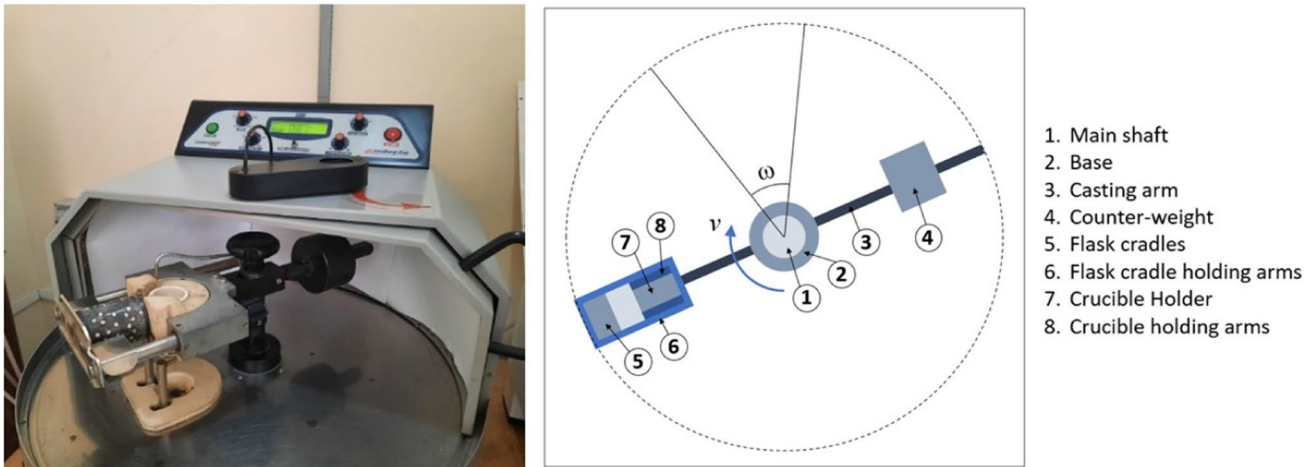


Fig. 6 Picture showing the inside of the PowerCast 1700 equipment and illustration of the centrifuge system used in the equipment

3 Virtual casting methodology

The computational modeling and simulation in this work will be carried out using the ProCAST software (ESI group) and its tools. The following sections detail the numerical simulation process, starting by the obtention of the casting crucible geometry.

3.1 Crucible and part modeling

Due to its complexity, the crucible geometry was digitized by a 3D scanner (Matter and Form Desktop 3D scanner). This scanner emits two red light beams that, once they reach the surface of the object to be digitized, are detected by the equipment camera and converted into digital points. The mesh representing the crucible is then generated from these points. Figure 8 shows the Matter and Form Desktop 3D Scanner digitizing the crucible geometry.

Assuming that the thickness of the real crucible is constant, the internal profile of the crucible was generated from the crucible external profile by a 3-mm offset operation in Autodesk Inventor. In this step, two different CAD geometries were designed. The first one was used in the simulations to obtain the IHTC for the gravity pouring process based on the work

of Konrad et al. [20], as previously described (Fig. 4). The second design was employed for the simulations of the filling (castability) elaborated based on the Whitlock methodology, initially presented in the study of Hinman et al. [18] and later mentioned in the work of Qiu et al. [19].

3.2 Discretization of the study domain and modeling

After producing the model geometry in Autodesk Inventor, ProCAST Visual-Mesh is used to discretize the domain of study by generating a mesh composed of tetrahedral elements, shown in Fig. 7.

Visual-CAST is the environment used to impose conditions on the process and feed the software the necessary input data to perform the calculations. Firstly, gravity direction is defined, and then, the material is set for each volume of the geometry, as well as the initial temperature and the percentage of initial filling of each material. For the mold (volume that will be filled), the initial filling is set at 0%, and for the crucible, a volumetric percentage compatible with the total mass needed to fill the part and the riser is imposed.

In the HTC Manager Interface tab, the user selects the type of contact between the parts. In this work, the COINC

Fig. 7 Mesh generated for analysis in ProCAST software. **a** Complete set: mold, part, and crucible. **b** Detail of the part mesh refinement

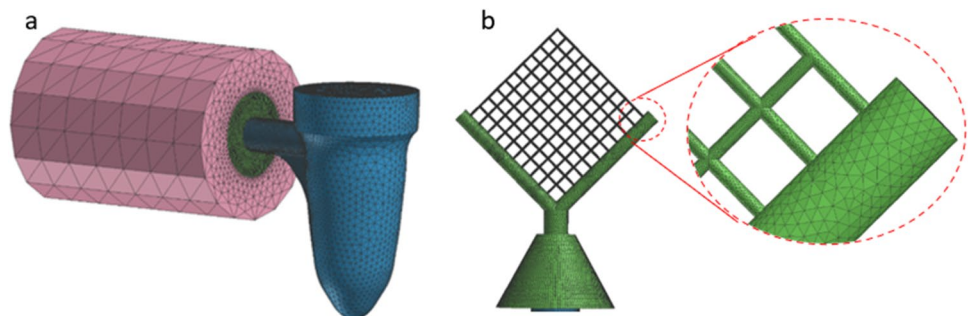


Table 2 Input data used in the simulations to estimate the IHTC by gravity pouring

Input data	Gravity pouring	Centrifugal pouring
Alloy	1, 2, and 3	
Mold	Refractory plaster Resincast	
Pouring method	Gravity	Centrifugal
Filling time (s)	2	(Not applicable)
Pouring temperature (T_{inj} in °C)	1158 (Alloy 1) 1255 (Alloy 2) 1272 (Alloy 4)	5 above liquidus temperature
Solidus temperature (°C)	Calculated for each alloy using CompuTherm	
Liquidus temperature (°C)	Calculated for each alloy using CompuTherm	
Mold temperature (°C)	Initially at 450	Constant at 420
Temperature outside the mold (°C)	Room temperature	
Coefficient of heat exchange between the mold and the environment ($W/m^2 K$)	Natural convection with 10	Forced convection with 65
IHTC (h_i in $W/m^2 K$)	Estimated for each alloy and mold assembly	895 (Alloy 1) 100 ($T < 880$ °C) (Alloy 2) 200 ($T > 1030$ °C) (Alloy 2) 535 (Alloy 3)
Cast alloy mass (g)	50	8
Distance between mold inlet and center of rotation (mm)	-	120

type contact was used at the contact between mold and metal. The COINC option doubles the nodes at the interface and allows to set different temperatures at each node location. This allows to represent the temperature drop between two different materials, such as the casting and the mold.

Boundary conditions such as thermal conditions of heat transfer, rotation geometry and fluid dynamics of pressure are created in the Process Condition Manager. Table 2 summarizes the input data used in all evaluated cases.

For the cases aiming the estimation of IHTC, the injection temperatures presented in Table 2 were imposed taking into account the acquisition made by the K-type thermocouple inserted in the center of the part and in contact with the alloy (T00). For the cases aiming the validation of the model, some data and input conditions are kept the same for each simulation and experiment, and some properties change depending on the alloy composition (e.g., pouring temperature). Therefore, in order to properly perform the validation comparison, it was necessary to create some standardized definition methods to impose these properties, thus generating similar simulation conditions.

Finally, the simulation parameters are imposed for a predefined centrifugal process, however with some modified parameters to better suit our specific case. Furthermore, besides the thermal and flow analysis provided by the ProCAST software, a turbulence module was used with a Realizable k-epsilon model, as it has already been proven in several experiments that the realizable k- ϵ model provides better accuracy for flows involving rotations, strong recirculation, or separation [22].

4 Model validation using Whitlock methodology

Model validation was carried out through the comparison with the casting and solidification parameters obtained from the Cu-Al-based manufactured parts. The geometry

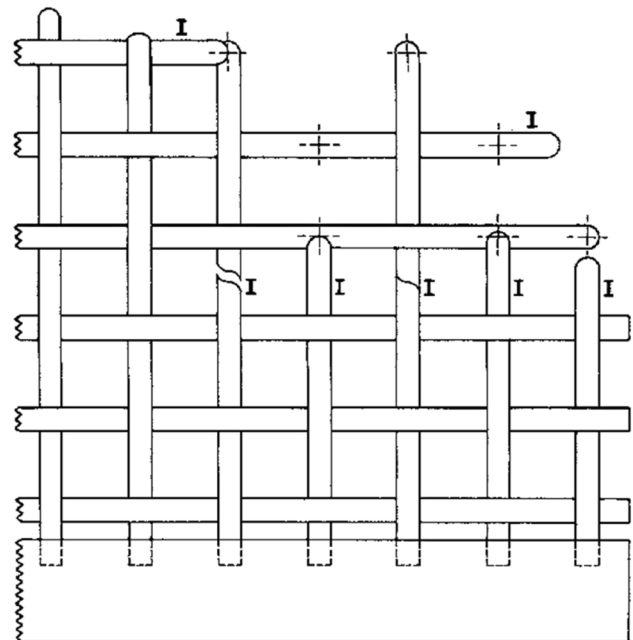


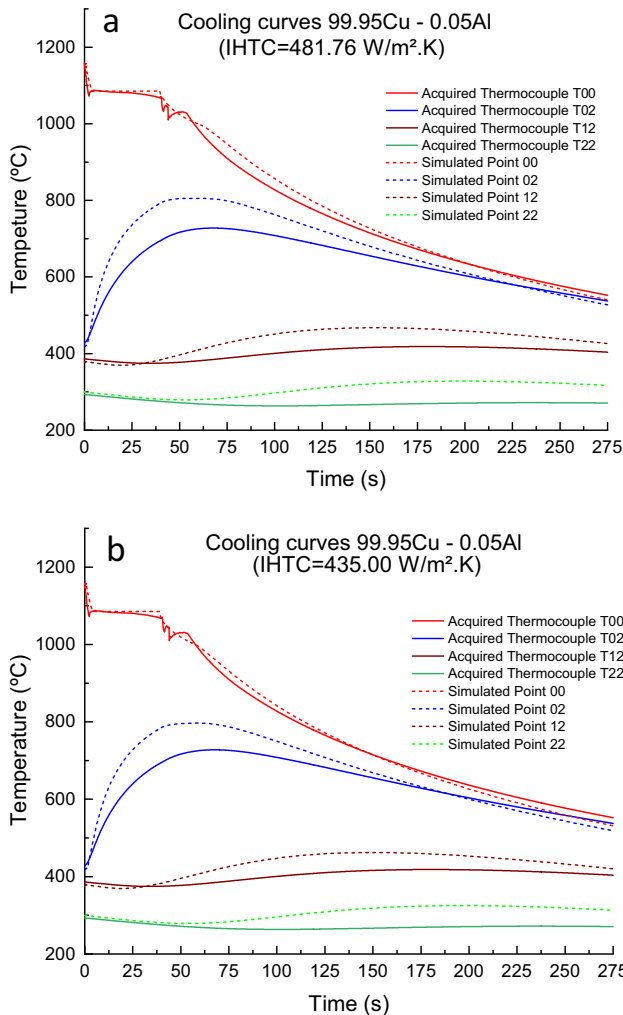
Fig. 8 Method for counting segments considered incomplete (I) in the Y 2D lattice part Hinman et al. [18]

Table 3 Average IHTC calculated for the studied alloys

Alloy	Composition	IHTC calculated with Eq. (1) (W/m ² K)
1	99.95Cu–0.05Al	481.76
2	97.40Cu–1.60Al	288.78
3	86.70Cu–7.90Al–5.40Mn	68.41

Table 4 Error and root-mean-square error (RMSE) between experimental and numerical cooling curves for alloy 1

IHTC (W/m ² K)	Error region 1 (%)	Error region 2 (%)	Error region 3 (%)	Total error (%)	RMSE (°C)
481.76	2.07	0.43	1.65	1.30	17.10
435.00	2.17	0.41	1.62	1.30	14.12

**Fig. 9** Experimental versus simulated cooling curves for alloy 1 with a IHTC = 481.76 W/m² K and b) IHTC = 435.00 W/m² K

of the specimen used for the validation is a Y 2D (shown in Fig. 1a) consisting of a grid with 100 open squares and 200 segments. This geometry is based on the Whitlock methodology, initially presented in the study of Hinman et al. [18] and later mentioned in the work of Qiu et al. [19].

Whitlock's methodology presents a simple counting procedure to assess castability through the counting of incomplete lattice segments. By observing the filling in the virtual

and real Y 2D parts, castability values are determined and compared. Equation 4 is used to quantify the castability (C) of the alloy.

$$C(\%) = \frac{(N_T - N_i)}{N_T} \times 100\% \quad (4)$$

where C is the castability, given as a percentage, N_T is the total number of segments in the Y 2D lattice part, and N_i is the number of incomplete segments after casting. The segment was considered incomplete (indicated by the letter "I") according to the illustration in Fig. 8.

5 Results and discussions

5.1 IHTC estimation from gravity pouring castings

The IHTC is an important parameter that describes the temperature drop in the melt and mold contact zone during solidification [20]. In numerical simulations of casting and solidification, IHTC is imposed as a boundary condition that must be either known or adequately approximated to allow results with a high degree of reliability.

During the process of pouring the alloy into the mold to manufacture the part shown in Fig. 4, temperature measurements were made at three points in the mold and one point in the alloy. After the acquisition of these temperatures and with the aid of Eqs. (1), (2), and (3), the IHTC values were calculated as a function of time. However, to enable a more general use these coefficients as reference values for future simulations, the IHTC of each assembly was considered constant, and for that it was necessary to calculate average values. According to O'Mahoney and Browne [23], this is a common approach, although we must be aware that the conditions at the alloy/mold interface did not remain constant throughout the solidification process.

Table 3 presents the calculated average IHTC values, suggesting that the IHTC decreased with the increase in aluminum content. Moreover, the manganese addition strongly affected the coefficient, presenting a 6-fold decreased compared to alloy 1.

The values presented in Table 3 were used as initial boundary conditions in an iterative process to determine

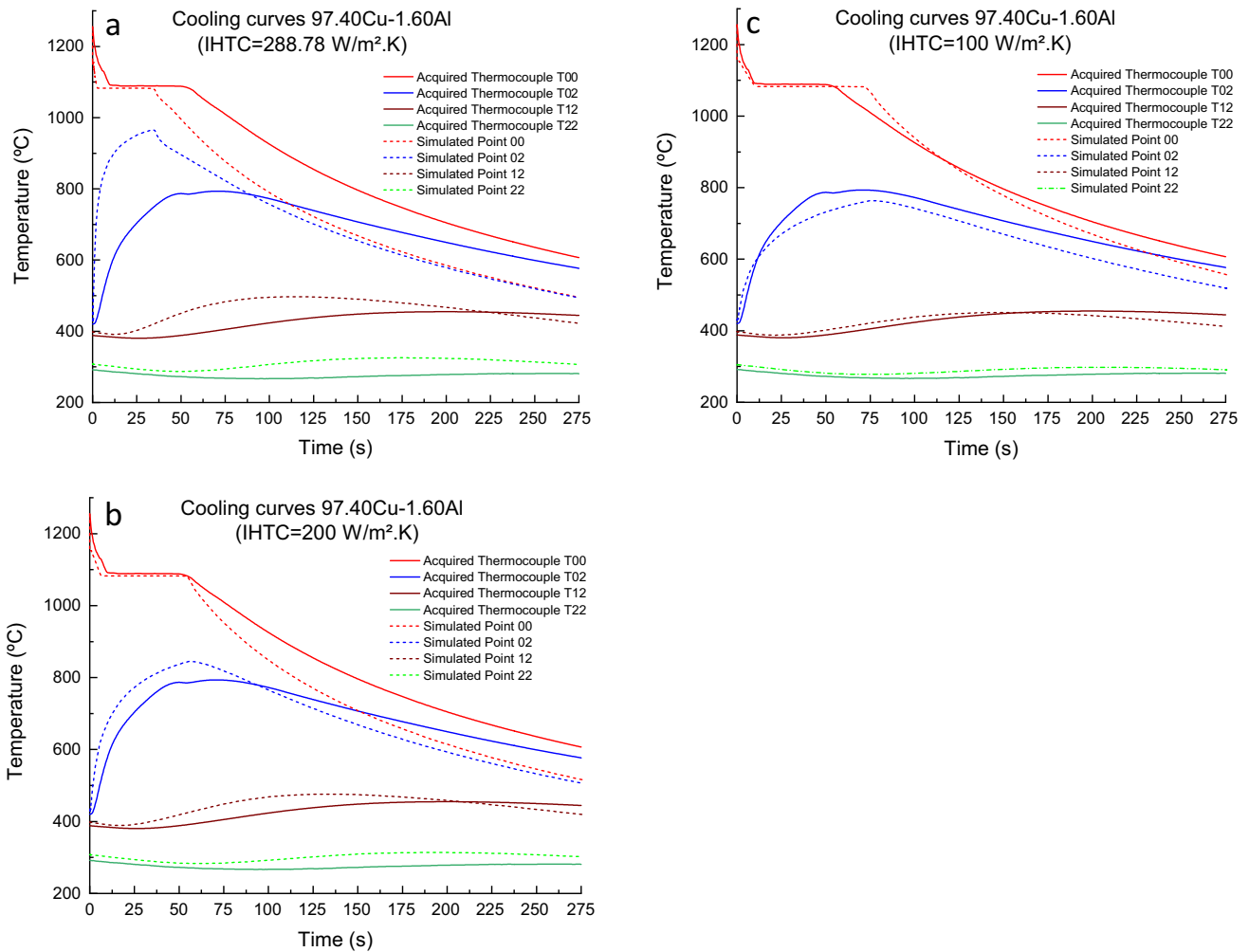


Fig. 10 Experimental versus simulated cooling curves for alloy 2 with **a** IHTC = 288.78 W/m² K, **b** IHTC = 200 W/m² K, and **c** IHTC = 100 W/m² K

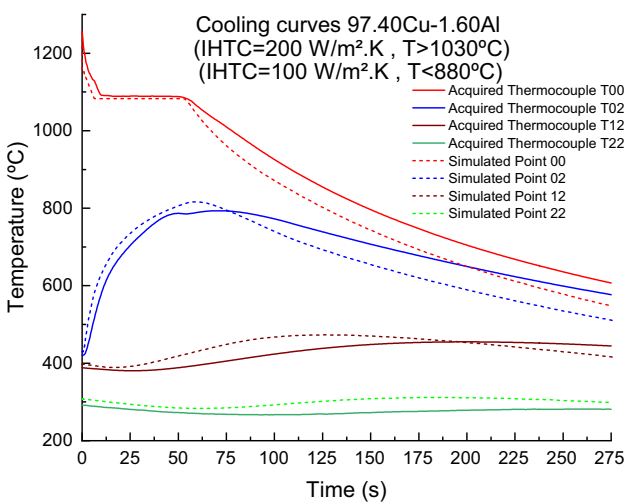


Fig. 11 Experimental versus simulated cooling curves for alloy 2 with IHTC = 100 W/m² K for T < 880 °C and IHTC = 200 W/m² K for T > 1030 °C

the IHTC for each alloy using the inverse method, similar to Konrad et al. [20], O’Mahoney and Browne [23], and Chen et al. [24] approaches. More details are given in the following.

5.1.1 IHTC for 99.95Cu–0.05Al (alloy 1)

Figure 9a compares the experimental and simulated cooling curves of alloy 1 in the plaster mold (geometry shown in Fig. 1b) with IHTC = 481.76 W/m² K, estimated by the average of the values calculated by Eq. 1, and showing a good approximation. The curve presents two points where the cooling rate changes sharply, dividing the curve in 3 distinct regions: region 1 is the cooling region before the phase transition; region 2 is where the phase transition temperatures are located, being a region of great importance for this study; and region 3 is associated with the alloy cooling

Table 5 Error and root-mean-square error (RMSE) between experimental and numerical cooling curves for alloy 2

IHTC (W/m ² K)	Error region 1 (%)	Error region 2 (%)	Error region 3 (%)	Total error (%)	RMSE (°C)
288.78	4.25	4.00	14.00	10.53	98.19
200	3.34	0.60	8.76	5.55	53.88
100	3.29	1.61	4.02	2.03	32.14
200 (<i>T</i> > 1030 °C) and 100 (<i>T</i> < 880 °C)	3.42	0.73	3.19	2.51	32.66

after solidification, associated with the formation of some defects such as hot spots and shrinkage porosities.

In order to improve and approximate the simulated and experimental curves, the IHTC value was iteratively refined. The approximation for alloy 1 started at 10 W/m² K above the reference value (481.76 W/m² K), presenting a greater divergence in relation to the experimental curves. Considering this result, the following simulations were carried out reducing 5 W/m² K from the previous value until reaching an optimal value. Figure 9b shows the simulation with IHTC = 435.00 W/m² K, which was the best obtained result.

Table 4 displays the errors calculated in the three regions of the cooling curves, the total error, and the root-mean-square error (RMSE). The percentage errors were obtained taking the experimental value as reference.

The total error for the two IHTC are the same. However, the RMSE is smaller for the optimized value of 435 W/m² K, thus presenting a smaller standard deviation. Another important point is that the percentage error of region 2 was lower for the optimized value. This is a region of interest, as it is where the alloy changes from liquid to solid phase.

5.1.2 IHTC for 97.40Cu–1.60Al (alloy 2)

Figure 10a shows the experimental cooling curves obtained with IHTC = 288.78 W/m² K, the estimated average of the values calculated by Eq. (1) for alloy 2. Although this averaged value was a good initial estimation, it is clear that this IHTC value is not adequate.

Figure 10b presents the results of simulation performed with IHTC = 200 W/m² K, leading to a better approximation up to 55 s of cooling. Afterwards, the simulated curve deviates significantly from the experimental curves. However, it is worth noting that after this time the alloy has already passed its solidus temperature (~1081 °C). Thus, the IHTC = 200 W/m² K for alloy 2 is considered good for simulations in this region. For the subsequent cooling, another IHTC value was optimized.

Figure 10c shows the simulation results for the IHTC = 100 W/m² K. In this case, the simulated curves approached the experimental curves of cooling after approximately 880 °C. However, there is a greater distance in the transition

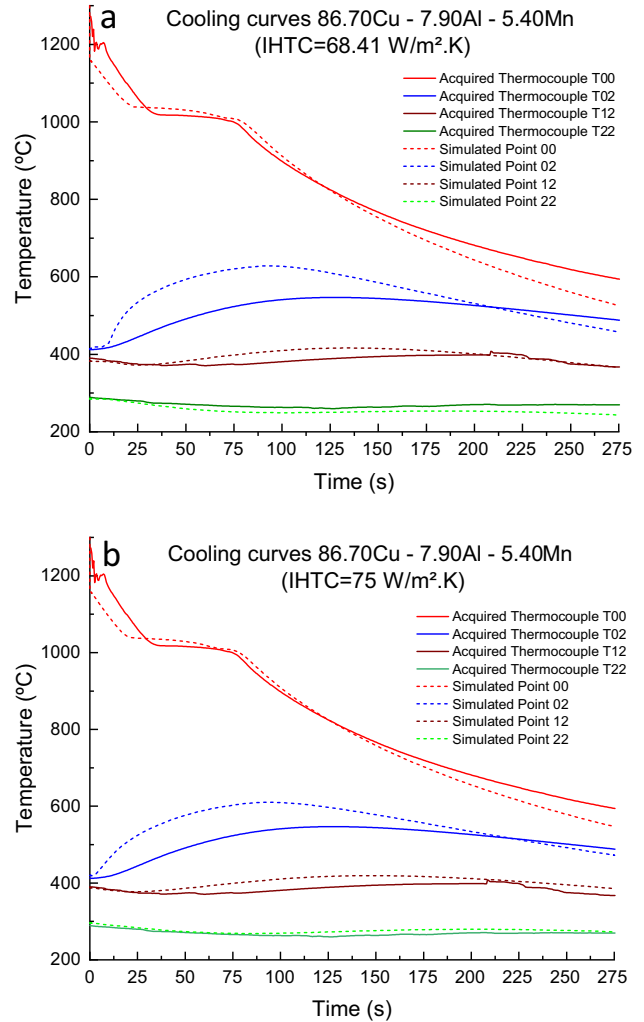


Fig. 12 Experimental versus simulated cooling curves for alloy 3 with **a** IHTC = 68.41 W/m² K and **b** IHTC = 75 W/m² K

Table 6 Error and root mean square error (RMSE) between experimental and numerical cooling curves for alloy 3

IHTC (W/m ² K)	Error region 1 (%)	Error region 2 (%)	Error region 3 (%)	Total error (%)	RMSE (°C)
68.41	5.54	1.18	5.30	4.16	43.76
75.00	5.78	1.16	2.31	2.53	35.37

Table 7 Castability measured for the studied cases

Alloy (% wt)	Simulated IHTC for gravity pouring (W/m ² K)	Simulated IHTC for centrifugal force (W/m ² K)	Castability (pouring temperature ~5 °C above liquidus temperature)	
			Experimental (%)	Virtual (%)
1 (99.95Cu–0.05Al)	435	895	34.50	33.50
2 (97.40Cu–1.60Al)	200 ($T > 1030$ °C) and 100 ($T < 880$ °C)	660 ($T > 1030$ °C) and 560 ($T < 880$ °C)	45.00	43.50
3 (86.70Cu–7.90Al–5.40Mn)	75	535	93.00	92.00

Table 8 Calculated Newtonian viscosity at 1100 °C of the studied alloys

Alloy (% wt)	Newtonian viscosity at 1100 °C (Pa s)
1 (99.95Cu–0.05Al)	0.00432021
2 (97.40Cu–1.60Al)	0.00395046
3 (86.70Cu–7.90Al–5.40Mn)	0.00266682

regions with this coefficient value. In order to further improve the approximation of the numerical and experimental results, an additional analysis was made using the two optimized IHTC values.

Figure 11 presents the simulation results of the cooling curves using IHTC = 200 W/m² K at temperatures above 1030 °C and IHTC = 100 W/m² K at temperatures below 880 °C. Since this result is better for the entire solidification and cooling processes, compared with the single IHTC curves shown in Fig. 10b and c, both averaged values were adopted in the analysis. The calculated errors in Table 5 reinforce this result.

5.1.3 IHTC for 86.7Cu–7.9Al–5.4Mn SMA (alloy 3)

Finally, Fig. 12 compares the experimental and simulated curves obtained with the averaged initially at IHTC = 68.41 W/m² K (Fig. 12a) and the optimized value 75 W/m² K for the Cu-Al-Mn SMA (Fig. 12b). The cooling curve with the optimized IHTC value presented a better approximation with the experimental curves, especially during solidification, from 993 to 1038 °C, and the final cooling.

The calculated errors shown in Table 6 for the IHTC estimation of the SMA (alloy 3) shows the improvement achieved with the optimized value in the general through the total error and RMSE, but especially for the region 3.

5.2 Model validation using the Whitlock methodology

The IHTC value depends on the conditions of the solidification process (vacuum, protective atmosphere, air, casting, and mold temperature), external pressure of the molten,

surface roughness of the mold and casting, and others [23]. In view of this, the IHTC previously determined needed to be adjusted for the centrifugal process evaluated in this research.

The adjustment was made iteratively, firstly comparing the castability of the experiment with the results of simulations of centrifugal casting for alloy 1 (99.95Cu–0.05Al). After defining the value of IHTC that provides a castability close to the experimental one, the difference between the IHTC obtained by gravity pouring simulation and the iteratively adjusted IHTC for the centrifugal casting is calculated. This identified difference was applied to the IHTC values obtained for alloys 2 and 3, thus making it possible to obtain an initial value for the adjustment simulations of the other alloys.

Table 7 summarizes the values of IHTC obtained via simulation for the gravity pouring process and for the centrifugal process, as well as the values of castability obtained by numerical simulations and experiments for the studied alloys.

From the data shown in Table 7, it can be noted that the change in process and geometry caused a substantial increase in IHTC. The difference between the estimated IHTC for the gravity pouring process of the plate sample and for the centrifugal process for the Y lattice part was 460 W/m² K for the three alloys.

The increase in the aluminum content generated a significant improvement in the castability for the evaluated investment casting process, for both real and virtual prototyping cases. This behavior was expected, since it is known that pure copper has a low melting capacity, generally leading to filling defects, surface cracks, and porosity problems [25]. Comparing alloy 1, with only 0.05% of aluminum, with alloy 3 with 7.9% aluminum and 5.4% manganese, there is an improvement of approximately 58.50% in the castability for both real and virtual castings. This significant increase observed in castability when adding aluminum or aluminum combined with manganese to copper is associated with an increase in the solidification interval and reduction of IHTC, which, in turn, decreases the cooling rate. According to [26], the castability is generally influenced by the shrinkage characteristics and cooling range of the alloy. Another characteristic that corroborates the improvement of castability with

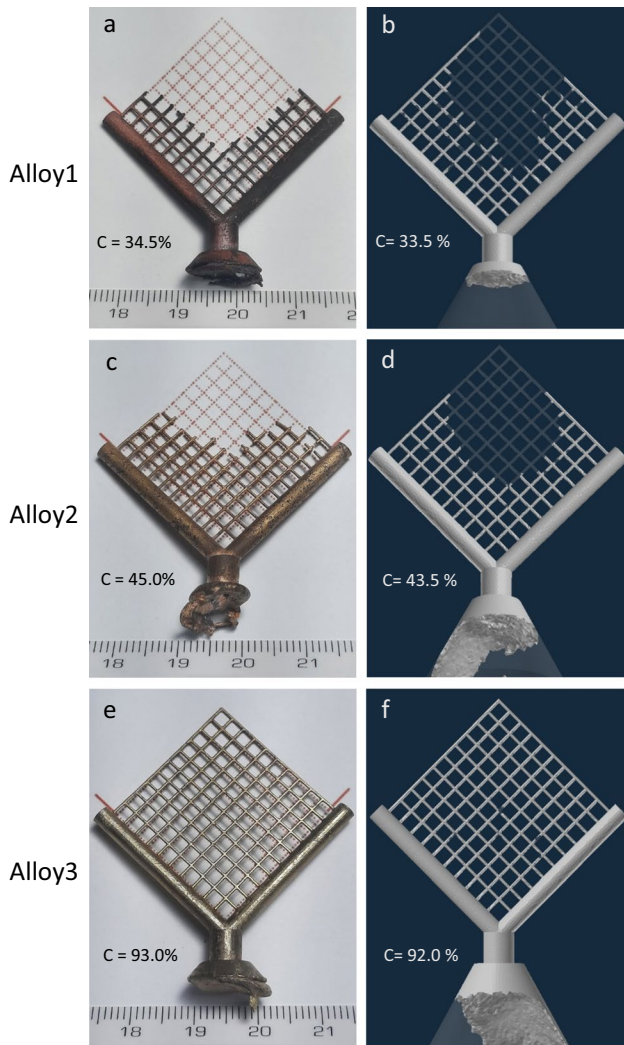


Fig. 13 Comparison of the lattice filling of segments with alloys 1, 2, and 3 at 5 °C above the liquidus temperature. **a, c, e** Real segment lattice part. **b, d, f** Virtual segment lattice part

the addition of these alloying elements is the reduction of Newtonian viscosity. Table 8 shows the theoretical viscosity values at 1100 °C calculated by ProCAST for each studied alloy.

Figure 13 compares the real and virtual prototyping of the Y lattice part with the centrifugal pouring investment casting process at an approximate temperature of 5 °C above the liquidus temperature of each alloy. Overall, the real measured castability was very close to the simulated cases, with maximum variations around 3%. The alloy 1, with the lowest aluminum content, has only 34.50% (real casting). The real part showed a more uniform fill with defects concentrated in the central region with two full segment sections close to the inlet channel. The virtual part showed a similar filling trend, but with a greater development of the peripheral segments and with some incomplete segments in the second line.

Similar to alloy 1, alloy 2 presented defects more centralized and directed to the edge of the Y lattice in the real case. For the case of virtual prototyping, the filling trend was towards the outermost regions with central defects, but also punctual defects in the segments of the second line section. The castability increased due to the higher amount of aluminum, reaching 45% in the real casting.

The casting of the copper-based SMA (alloy 3) was the best achieved, reaching 93% in the real casting. The defects presented in the real part were concentrated in the central-left region. In the virtual part, the defects appeared in two nodes in the center, in two nodes on the left and one node on the right of the part. Figure 14 shows in more detail the filling problems observed in alloy 3.

5.3 Segment network solidification time

It was possible to verify during the validation of the model that the addition of aluminum and/or aluminum and manganese in the pure copper influence the value of IHTC. It is known that this parameter has a strong relationship with the cooling rate, which, in turn, influences the castability, solidification kinetics, and the resulting microstructure [17].

Taking into account the importance of this information, this section will present an analysis of the solidification time for each alloy in order to verify the influence that these alloy

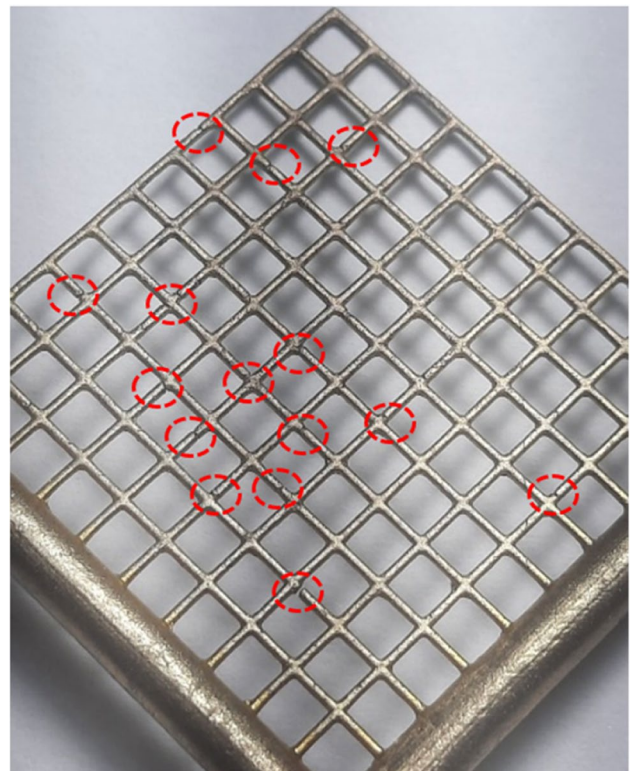
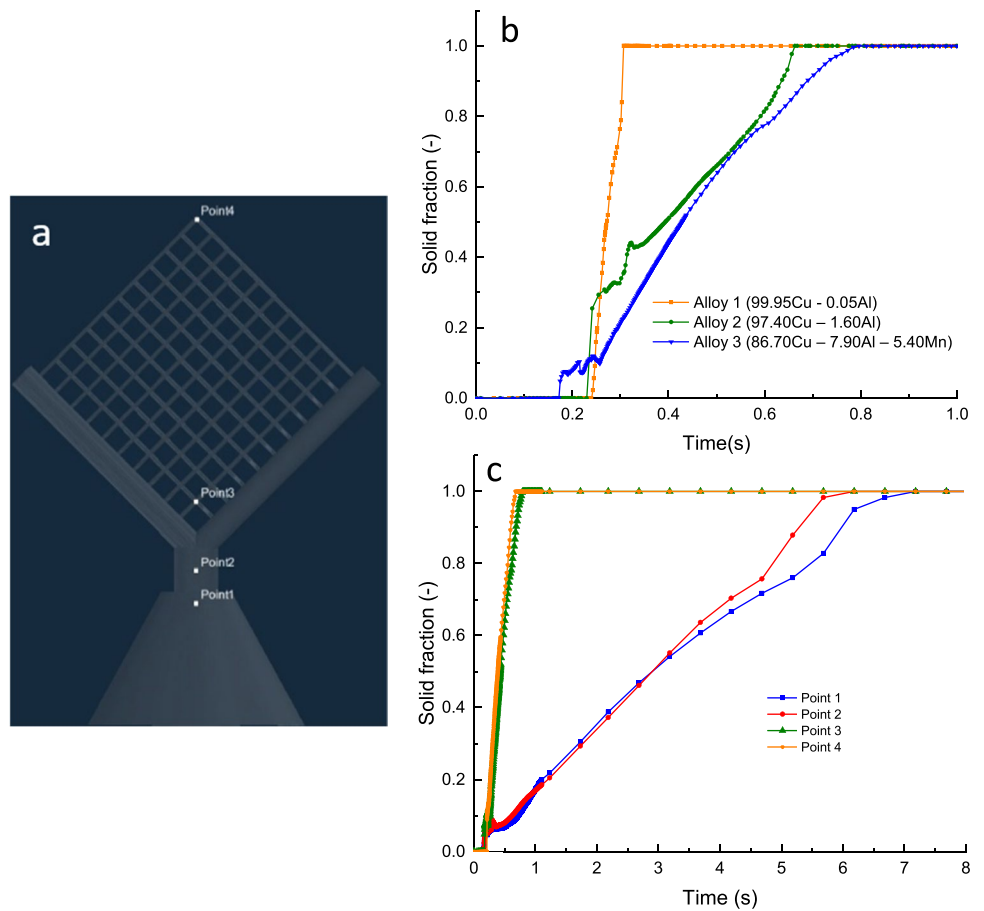


Fig. 14 Details of the filling failures for alloy 3 poured at 5 °C above the liquidus temperature

Fig. 15 **a** Selected points for the analysis of solidification time. **b** Solid fraction versus time curves for point 3 alloys 1, 2, and 3. **c** Solid fraction versus time curves for points 1, 2, 3, and 4 between 0 and 8 s for alloy 3



elements have on the solidification of the part. To carry out this evaluation, 4 points were defined on the Y lattice part. Figure 15a shows the location of these points. Due to the lack of filling in some cases, results in point 4 were not observed.

Table 9 summarizes the solidification time for each alloy with centrifugal pouring at a temperature of 5 °C above the liquidus temperature.

It is possible to identify that the solidification time at all evaluated points becomes greater with the increase of aluminum (alloy 2) and aluminum and manganese content (alloy 3). Graphically, we can visualize this effect in the

curves presented in Fig. 15b. These curves show that the cooling rate of alloy 1 is much higher than that of alloys 2 and 3 and that alloy 3 has the lowest cooling rate, probably associated to the lowest IHTC.

It is also possible to observe from the data in Table 9 that the difference in solidification times between points 1 and 2 for alloys 2 and 3 is 1 s, but for alloy 1, it is 0.22 s. Probably, this occurs due to the lack of material in the riser, as the alloy 2 and 3 have a more filled riser and thus have a greater amount of mass, generating a greater thermal load to be dissipated. Moreover, the parts have different solidification times depending on the evaluated point. Points closer to the entrance gate have a lower solidification rate, as noted by comparing the solidification times of the farthest points (point 1 and point 4) for alloy 3, with a difference of 6.50 s.

Moreover, the curves in Fig. 15c present the solid fraction evolution with time at the evaluated points between 0 and 8 s for alloy 3, showing the difference in cooling rates between the evaluated points. Points 4 and 3 show a similar behavior profile with a high solidification rate,

Table 9 Solidification times for centrifugal pouring with temperature 5 °C above the liquidus temperature

Alloy	Solidification time (s)			
	Point 1	Point 2	Point 3	Point 4
1 (99.95Cu–0.05Al)	1.76	1.54	0.31	-
2 (97.40Cu–1.60Al)	5.88	4.88	0.66	-
3 (86.70Cu–7.90Al–5.40Mn)	7.18	6.18	0.81	0.68

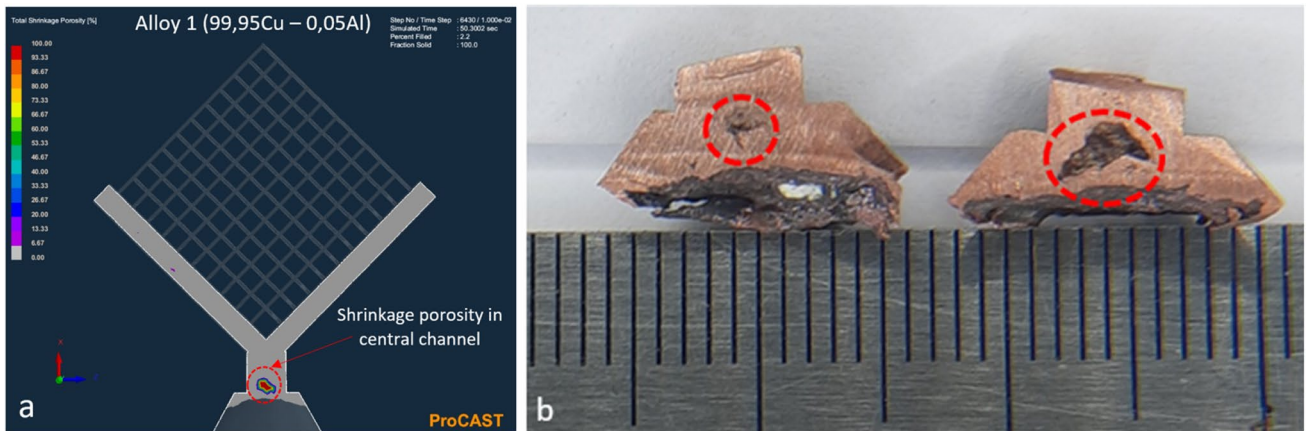


Fig. 16 **a** Section of the virtual casting of alloy 1 showing a porosity region. **b** Section of the real casting showing the internal cavity formed by shrinkage during cooling of alloy 1

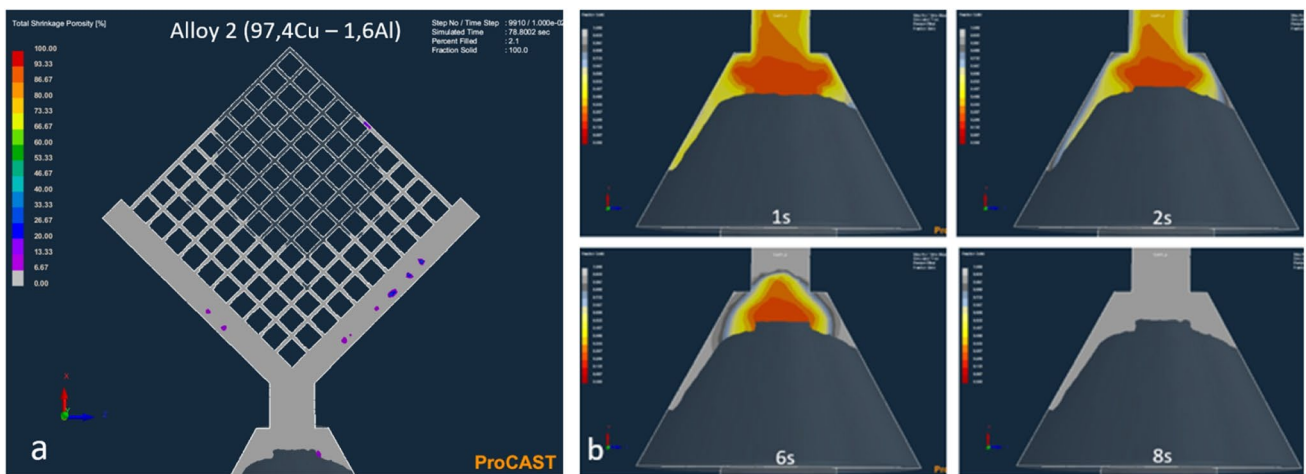


Fig. 17 **a** Section of the virtual casting of alloy 2 showing porosity regions. **b** Evolution riser contraction and cavity development in alloy 2

related to the low amount of mass present in these regions, leading to a greater ease of losing heat and solidifying.

5.4 Shrinkage porosity

The most critical regions regarding the presence of shrinkage porosities were identified in the virtual parts using sectional planes. The real parts were then sectioned at these

Fig. 18 Cavity formed by shrinkage in alloy 2 **(a)** before and **(b)** after sectioning

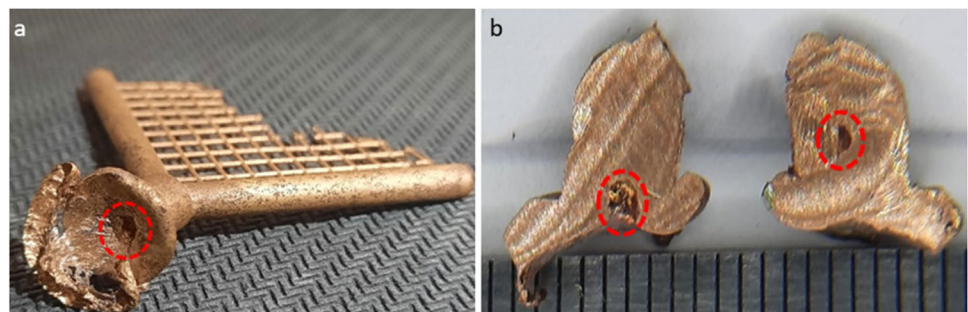


Fig. 19 **a** Section of the virtual casting of alloy 3 predicting a porosity region. **b** Section of the real casting showing no visual defects



identified regions. Figure 16 shows the regions that present shrinkage porosities in the virtual and real parts obtained by centrifugal casting with alloy 1. The virtual part presented a 7% contraction porosity in the right inlet channel and a more substantial contraction next to the riser (Fig. 16a). The real sectioned part of alloy 1 indeed presents a significant porosity in this region (Fig. 16b), which clearly is caused by the contraction of the cooling alloy due to its irregular cavity.

For the alloy 2, obtained by centrifugal pouring at 5 °C above the liquidus temperature, the virtual prototyping showed some points with shrinkage porosity of up to 23% located in the two feed channels. These regions can be seen in Fig. 17a. In this case, a cavity generated by the contraction of the riser was also identified. Figure 17b shows the riser contraction and cavity development at different instants.

This shrinkage behavior signaled by the virtual prototyping is confirmed in the real part manufactured with alloy 2, as shown in Fig. 18. Inspecting the part before the sectioning, it is possible to observe the presence of a contraction cavity in the riser (Fig. 18a). The sectioned part reveals the depth of this cavity as well as a new cavity in the central feed channel (Fig. 18b).

For the alloy 3, in Fig. 19a, the virtual prototyping indicated the appearance of shrinkage porosities of up to 66% in the central feed channel. However, as can be seen in Fig. 19b, when sectioning the real part no cavity is observed. A hypothesis for this divergence is that the shrinkage porosities indicated by the software appear in alloy 3 instead in the form of microporosities. Generally speaking, microporosity in alloys is a result of incomplete feeding into the pasty zone; i.e., the volume contraction associated with solidification cannot be compensated for by the interdendritic liquid flowing in opposition to the displacement of the isotherms [27, 28]. Pure metals and metallic alloys with a small solidification interval, as in the case of alloys 1 and 2, have small dendrites in the pasty zone that favor the formation of macroporosities when contraction occurs, while metallic alloys with a large solidification interval, similar to alloy 3, have large dendrites at the liquid/solid interface, which favors the formation of microporosities that often cannot be seen with the naked eye [17, 29].

6 Conclusions

Virtual prototyping was used to simulate a modified investment casting process where centrifugal force is applied to inject the melt into the mold. The modified process was simulated in the ProCAST software and enabled the study of castability, solidification and porosity for copper-based alloys, including a Cu-Al-Mn shape memory alloy (SMA). Regarding the performed analysis, the following conclusions are drawn:

- The addition of aluminum and manganese to copper to obtain a Cu-based shape memory alloys causes a reduction in the IHTC, leading to a reduction in the cooling rate;
- Compared to the gravity casting process, the centrifugal casting increases the IHTC significantly. For Cu-Al-Mn SMA (alloy 3), a 7-fold increase was observed; for aluminum bronze (alloy 2), a 3-fold increase was observed, and for near-pure copper (alloy 1), a 2-fold increase was observed;
- The assumption that the IHTC is constant for the functional Cu-Al-Mn SMA is a simplification that does not negatively affect the approximation of the actual cooling conditions of the alloy;
- The addition of aluminum and manganese considerably improved the castability of the copper-based alloys;
- The 86.7Cu–7.9Al–5.4Mn SMA, the composition of greatest interest for this work, presents a high castability and a low cooling rate.

This study also enabled, through data collection such as IHTC and model validation, the use of commercial software to design and analyze a casting process that differs from traditional centrifugal casting method, in which the molten metal is poured in the same direction as the axis of rotation. It is worth noting that the proposed and performed analysis is not yet part of the ProCAST software scope and, therefore, potentially serves as basis for new virtual processing routes. Furthermore, the analysis benefits the design of new complex casting systems such as axisymmetric or non-symmetrical parts manufactured with functional CuAlMn

SMA. The increased efficiency achieved by virtual prototyping of the investment casting process is possible through the analysis of mold filling, temperature gradients, solidification time, and development of contraction porosities before real castings are manufactured.

Acknowledgements The authors acknowledge to the authors cited in the text which helped in the improvement of this paper, as well as the ESI Group for granting the license to the ProCAST program (Ref: CA/ARDS/RSD_2007_01BR).

Author contributions Carlos Eduardo da Silva Albuquerque: conceptualization, methodology, software, writing original draft, investigation, formal analysis. Estephanie Nobre Dantas Grassi: conceptualization, validation, writing review and editing. Carlos Jose de Araujo: conceptualization, validation, project administration, supervision, funding acquisition. All authors read and approved the final manuscript.

Funding This research was funded by the Brazilian National Council for Scientific and Technological Development (CNPq) projects: National Institute of Science and Technology-Smart Structures in Engineering, grant number 574001/2008-5; Universal 2016, grant number 401128/2016-4; and PQ-1C, grant number 302740/2018-0. The Brazilian Coordination of Superior Level Staff Improvement (CAPES) for the post-doctoral scholarship (88887.355150/2019-00) granted to the author Estephanie Nobre Dantas Grassi.

Declarations

Conflict of interest The authors declare no competing interests.

References

- Rao A, Srinivasa AR, Reddy JN (2015) Design of shape memory alloy (LMF) Actuators. Springer, New York
- Malik V, Srivastava S, Gupta S, Sharma V, Vishnoi M, Mamatha TG (2021) A novel review on shape memory alloy and their applications in extraterrestrial roving missions. *Mater Today Proc* 44:4961–4965. <https://doi.org/10.1016/j.matpr.2020.12.860>
- Khoshlahjeh M, Barbarino S, Ameduri S (2021) Shape memory alloy applications for helicopters. In: Concilio A, Antonucci V, Auricchio F, Lecce L, Sacco E (eds) *Shape Mem Alloy Eng Aerospace, Struct Biomed Appl*, 2nd edn. Elsevier, pp 591–607. <https://doi.org/10.1016/B978-0-12-819264-1.00017-0>
- Auricchio F, Boatti E, Conti M (2015) SMA Biomedical Applications. In: Concilio A (ed) L.L. Butterworth-Heinemann, *Shape Mem. Alloy Eng.*, pp 307–341. <https://doi.org/10.1016/B978-0-08-099920-3.00011-5>
- Bahraminasab M, Bin Sahari B (2013) NiTi shape memory alloys, Promising Materials in Orthopedic Applications, in: *Shape Mem. Alloy. - Process. Charact. Appl.*, pp. 261–278. <https://doi.org/10.5772/52228>
- Prymak O, Klocke A, Kahl-Nieke B, Epple M (2004) Fatigue of orthodontic nickel-titanium (NiTi) wires in different fluids under constant mechanical stress. *Mater Sci Eng A* 378:110–114. <https://doi.org/10.1016/j.msea.2003.10.332>
- Gheorghita V, Gumpel P, Strittmatter J, Anghel C, Heitz T, Senn M (2013) Using shape memory alloys in automotive safety systems. In: Springer. Berlin Heidelberg, pp 909–917. https://doi.org/10.1007/978-3-642-33835-9_83
- Williams EA, Shaw G, Elahinia M (2010) Control of an automotive shape memory alloy mirror actuator. *Mechatronics* 20:527–534. <https://doi.org/10.1016/j.mechatronics.2010.04.002>
- Zareie S, Issa AS, Seethaler RJ, Zabihollah A (2020) Recent advances in the applications of shape memory alloys in civil infrastructures: a review. *Structures* 27:1535–1550. <https://doi.org/10.1016/j.istruc.2020.05.058>
- Peairs DM, Park G, Inman DJ (2004) Practical issues of activating self-repairing bolted joints. *LMF Mater Struct* 13:1414–1423. <https://doi.org/10.1088/0964-1726/13/6/012>
- Agrawal A, Dube RK (2018) Methods of fabricating Cu-Al-Ni shape memory alloys. *J Alloys Comp* 750:235–247. <https://doi.org/10.1016/j.jallcom.2018.03.390>
- Khan MAA, Sheikh AK (2018) Comparative study of simulation software for modelling metal casting processes. *Int J Simulat Model* 17:197–209. [https://doi.org/10.2507/IJSIMM17\(2\)402](https://doi.org/10.2507/IJSIMM17(2)402)
- Tao P, Shao H, Ji Z, Nan H, Xu Q (2018) Numerical simulation for the investment casting process of a large-size. *Progr Nat Sci: Mater Int* 28:520–528. <https://doi.org/10.1016/j.pnsc.2018.06.005>
- Kumar R, Madhu S, Aravindh K, Jayakumar V, Bharathiraja G, Muniappa A (2020) Casting design and simulation of gating system in rotary adaptor using procast software for defect minimization. *Mater Today: Proc* 22:799–805. <https://doi.org/10.1016/j.matpr.2019.10.156>
- Dou K, Lordan E, Zhang YJ, Jacot A, Fan ZY (2019) Numerical simulation of fluid flow, solidification and defects in high pressure die casting (HPDC) process. In: *IOP Conf. Series: Materials Science and Engineering* 529, Salzburg, Austria. <https://doi.org/10.1088/1757-899X/529/1/012058>
- Allison J, Li MC, Wolverson C, Su XM (2006) Virtual aluminum castings: an industrial application of ICME. *JOM* 58:28–35. <https://doi.org/10.1007/s11837-006-0224-4>
- Garcia A (2007) *Solidificação: Fundamentos e Aplicações*. 2ª Edição. Editora Unicamp, São Paulo
- Hinman RW, Tesk JA, Whitlock RP, Parry EE, Durkowski JS (1985) Technique for characterizing casting behavior of dental alloys. *J Dental Res* 64:134–138. <https://doi.org/10.1177/00220345850640020801>
- Qiu KJ, Lin WJ, Zhou FY, Nan HQ, Wang BL, Li L, Lin JP, Zheng YF, Liu YH (2014) Ti–Ga binary alloys developed as potential dental materials. *Materials Science and Engineering: C* 34:474–483. <https://doi.org/10.1016/j.msec.2013.10.004>
- Konrad CH, Brunner M, Kyrgyzbaev K, Vokl R, Glatzel IJ (2011) Determination of heat transfer coefficient and ceramic mold material parameters for alloy IN738LC investment castings. *J Mater Process Technol* 211:181–186. <https://doi.org/10.1016/j.jmatprotec.2010.08.031>
- Mun J, Busse M, Ju J, Thurman J (2015) Multilevel metal flow-fill analysis of centrifugal casting for indirect additive manufacturing of lattice structures. *Proceedings of the ASME 2015 International Mechanical Engineering Congress and Exposition*. Volume 2A: Advanced Manufacturing. Houston, Texas, USA. <https://doi.org/10.1016/j.jmatprotec.2010.08.031>
- ESI (2019) ProCast Casting Simulation Suite. ProCAST User's Guide. ESI software, France
- O'Mahoney D, Browne DJ (2000) Use of experiment and an inverse method to study interface heat transfer during solidification in the investment casting process. *Exp Thermal Fluid Sci* 22:111–122. [https://doi.org/10.1016/S0894-1777\(00\)00014-5](https://doi.org/10.1016/S0894-1777(00)00014-5)
- Chen L, Wang Y, Peng L, Fu P, Jiang H (2014) Study on the interfacial heat transfer coefficient between AZ91D magnesium alloy and silica sand. *Exp Ther Fluid Sci* 54:196–203. <https://doi.org/10.1016/j.expthermflusci.2013.12.010>

25. ASM(2008) Handbook casting: casting of copper and copper alloys. ASM International. All Rights Reserved.15:1026- 1044. <https://doi.org/10.31399/asm.hb.v15.9781627081870>
26. ASM (2004) Handbook metallography and microstructures: metallography and microstructures of copper and its alloys. ASM International. All Rights Reserved 9: 775 - 780 Ohio. <https://doi.org/10.31399/asm.hb.v09.9781627081771>
27. Liu Y, Jie W, Gao Z, Zheng Y (2015) Investigation on the formation of microporosity in aluminum alloys. J Alloys Comp 629:221–229. <https://doi.org/10.1016/j.jallcom.2015.01.009>
28. Doru MS (2009) Science and engineering of casting solidification, Second edn. The Ohio State University, Columbus
29. Dantzig JA, Rappaz M (2016) Solidification. 2ª Edição. EPFL Press, Chicago <http://solidification.mechanical.illinois.edu/Book/index.html>

Publisher's note Springer Nature remains neutral with regard to jurisdictional claims in published maps and institutional affiliations.

Springer Nature or its licensor (e.g. a society or other partner) holds exclusive rights to this article under a publishing agreement with the author(s) or other rightsholder(s); author self-archiving of the accepted manuscript version of this article is solely governed by the terms of such publishing agreement and applicable law.